

Emerging SARS-CoV-2 variants expand species tropism to rodents

Huiping Shuai

University of Hong Kong

Jasper Chan

The University of Hong Kong <https://orcid.org/0000-0001-6336-6657>

Terrence Tsz-Tai Yuen

University of Hong Kong

Chaemin Yoon

The University of Hong Kong

Jingchu Hu

Shenzhen Institutes of Advanced Technology <https://orcid.org/0000-0001-6144-7226>

Lei Wen

University of Hong Kong

Bingjie Hu

University of Hong Kong

Dong Yang

University of Hong Kong

Yixin Wang

University of Hong Kong

Yuxin Hou

University of Hong Kong

Xiner Huang

The University of Hong Kong <https://orcid.org/0000-0002-0154-8372>

Yue Chai

University of Hong Kong

Chris Chan

The University of Hong Kong <https://orcid.org/0000-0001-7089-4829>

Vincent Poon

The University of Hong Kong

Rui-Qi Zhang

University of Hong Kong

Wan-Mui Chan

University of Hong Kong

Jonathan Daniel Ip

University of Hong Kong

Allen Wing Ho Chu

University of Hong Kong

Ye-fan Hu

University of Hong Kong

Jian-Piao Cai

University of Hong Kong

Kwok-Hung Chan

The University of Hong Kong

Jie Zhou

University of Hong Kong <https://orcid.org/0000-0002-2948-3873>

Siddharth Sridhar

The University of Hong Kong

Bao-Zhong Zhang

University of Hong Kong

Shuofeng Yuan

University of Hong Kong <https://orcid.org/0000-0001-7996-1119>

Jinxia Zhang

Department of microbiology <https://orcid.org/0000-0002-5087-3614>

Jiandong Huang

The University of Hong Kong <https://orcid.org/0000-0001-7531-2816>

Kelvin To

The University of Hong Kong <https://orcid.org/0000-0002-1921-5824>

Kwok-Yung Yuen

The University of Hong Kong <https://orcid.org/0000-0002-2083-1552>

Hin Chu (✉ hinchu@hku.hk)

The University of Hong Kong <https://orcid.org/0000-0003-2855-9837>

Article

Keywords: SARS-CoV-2 variants, rodents, ACE2

Posted Date: July 13th, 2021

DOI: <https://doi.org/10.21203/rs.3.rs-676992/v1>

License:   This work is licensed under a Creative Commons Attribution 4.0 International License.

[Read Full License](#)

1 **Title:**

2 Emerging SARS-CoV-2 variants expand species tropism to rodents

3

4 **Authors:**

5 Huiping Shuai^{1,2,3,*}, Jasper Fuk-Woo Chan^{1,2,3,4,5,#,*}, Terrence Tsz-Tai Yuen^{2,*}, Chaemin
6 Yoon², Jing-Chu Hu⁶, Lei Wen², Bingjie Hu², Dong Yang², Yixin Wang², Yuxin Hou², Xiner
7 Huang², Yue Chai², Chris Chung-Sing Chan², Vincent Kwok-Man Poon², Rui-Qi Zhang²,
8 Wan-Mui Chan², Jonathan Daniel Ip², Allen Wing-Ho Chu², Ye-Fan Hu⁷, Jian-Piao Cai²,
9 Kwok-Hung Chan^{1,2,3}, Jie Zhou^{1,2,3}, Siddharth Sridhar^{1,2,3}, Bao-Zhong Zhang⁶, Shuofeng
10 Yuan^{1,2,3}, Anna Jinxia Zhang^{1,2,3}, Jian-Dong Huang^{6,7}, Kelvin Kai-Wang To^{1,2,3,5}, Kwok-
11 Yung Yuen^{1,2,3,4,5,#}, Hin Chu^{1,2,3,#}

12

13 **Affiliations:**

14 ¹State Key Laboratory of Emerging Infectious Diseases, Li Ka Shing Faculty of Medicine,
15 The University of Hong Kong, Pokfulam, Hong Kong Special Administrative Region, China.

16 ²Department of Microbiology, Li Ka Shing Faculty of Medicine, The University of Hong
17 Kong, Pokfulam, Hong Kong Special Administrative Region, China

18 ³Carol Yu Centre for Infection, Li Ka Shing Faculty of Medicine, The University of Hong
19 Kong, Pokfulam, Hong Kong Special Administrative Region, China

20 ⁴Department of Microbiology, Queen Mary Hospital, Pokfulam, Hong Kong Special
21 Administrative Region, China

22 ⁵Hainan Medical University-The University of Hong Kong Joint Laboratory of Tropical
23 Infectious Diseases, The University of Hong Kong, Pokfulam, Hong Kong Special
24 Administrative Region, China

25 ⁶Synthetic Biology, Shenzhen Institutes of Advanced Technology, Chinese Academy of
26 Sciences; Shenzhen, People's Republic of China

27 ⁷School of Biomedical Sciences, Li Ka Shing Faculty of Medicine, The University of Hong
28 Kong; Pokfulam, Hong Kong Special Administrative Region, China

29 *These authors contributed equally as co-first authors

30

31 **#Correspondence:** Hin Chu (hinchu@hku.hk), Kwok-Yung Yuen (kyyuen@hku.hk), and
32 Jasper Fuk-Woo Chan (jfwchan@hku.hk). State Key Laboratory of Emerging Infectious
33 Diseases, Carol Yu Centre for Infection, Department of Microbiology, Li Ka Shing Faculty
34 of Medicine, The University of Hong Kong, Pokfulam, Hong Kong Special Administrative
35 Region, China. Tel: 852-22552402. Fax: 852-28551241.

36

37

38 **Abstract**

39 Mice are not susceptible to wildtype SARS-CoV-2 infection. Emerging SARS-CoV-2
40 variants including B.1.1.7, B.1.351, P.1, and P.3 contain mutations in spike, which have been
41 suggested to associate with an increased recognition of mouse ACE2, raising the postulation
42 that they may have evolved to expand species tropism to rodents. Here, we investigated the
43 capacity of B.1.1.7 and other emerging SARS-CoV-2 variants in infecting mouse (*Mus*
44 *musculus*) and rats (*Rattus norvegicus*) under *in vitro* and *in vivo* settings. Our results show
45 that B.1.1.7 and P.3, but not B.1 or wildtype SARS-CoV-2, can utilize mouse and rat ACE2
46 for virus entry *in vitro*. High infectious virus titers, abundant viral antigen expression, and
47 pathological changes are detected in the nasal turbinate and lung of B.1.1.7-inoculated mice
48 and rats. Together, these results reveal that the current predominant circulating SARS-CoV-2
49 variant, B.1.1.7, has gained the capability to expand species tropism to rodents.

50

51 **Introduction**

52 Coronaviruses have repeatedly crossed species barriers to cause human infection ¹. Severe
53 acute respiratory syndrome coronavirus 2 (SARS-CoV-2) is a novel lineage B human-
54 pathogenic betacoronavirus that was first identified in December 2019 ². SARS-CoV-2 is
55 highly transmissible and has rapidly spread worldwide to cause more than 180 million cases
56 of Coronavirus Disease 2019 (COVID-19) with over 3.9 million deaths ^{3,4}. Same as SARS-
57 CoV-2 and human coronavirus NL63 (HCoV-NL63), SARS-CoV-2 also uses angiotensin-
58 converting enzyme II (ACE2) as the cellular receptor for entry ⁵. Importantly, new SARS-
59 CoV-2 variants of concern (VOC) with amino acid substitutions at the receptor-binding
60 domain of spike protein continue to emerge as the pandemic expands and are potentially
61 associated with increased transmissibility and/or virulence ⁶.

62

63 Mammals, especially bats and rodents, are considered to be the main animal reservoirs of
64 alphacoronaviruses and betacoronaviruses ^{1,7}. The global distribution, rapid growth rate, high
65 population densities, and close peridomestic relationship with humans of synanthropic rodent
66 species like rats and mice give them important roles in the transmission cycle of various
67 zoonotic pathogens ⁸⁻¹⁰. We and others have previously shown that murine cells are not
68 susceptible to SARS-CoV-2 infection *in vitro* and mice are not infectable by SARS-CoV-2 *in*
69 *vivo* ^{11,12}, which is due to the amino acid substitutions present at the ACE2-spike interacting
70 surface on mouse ACE2 (mACE2) compared with human ACE2 (hACE2) that render SARS-
71 CoV-2 spike unable to utilize mACE2 for cell entry ^{13,14}. Interestingly, emerging SARS-
72 CoV-2 variants, including B.1.1.7 ⁶, B.1.351 ¹⁵, P.1 ¹⁶, and P.3 ¹⁷, all contain the N501Y
73 mutation in spike that has been suggested to be associated with mouse adaptation ¹⁸, raising
74 the postulation that these emerging SARS-CoV-2 variants may have evolved to expand
75 species tropism to mouse and possibly other rodents. To evaluate this possibility with major

76 public health significance, we in parallel evaluated the capacity of SARS-CoV-2 wildtype
77 (WT) and SARS-CoV-2 B.1.1.7 variant to infect mice (*Mus musculus*) and rats (*Rattus*
78 *norvegicus*). Our results demonstrate that while mice and rats are not permissive to WT
79 SARS-CoV-2, B.1.1.7 efficiently infects these rodents with production of infectious virus
80 particles in the nasal turbinate and lung for 4-to-7 days post infection. These findings indicate
81 that the predominant circulating SARS-CoV-2 variant, B.1.1.7, have gained the capacity to
82 expand species tropism to rodents and that public health control measures including stringent
83 rodent control should be implemented to facilitate the control of the ongoing pandemic.

84

85 **Results**

86 **The predominant circulating SARS-CoV-2 variant B.1.1.7 efficiently infects mice**

87 B.1.1.7 emerged in late 2020 and has quickly become the dominant SARS-CoV-2 variant
88 among all recently reported SARS-CoV-2 isolates in countries on different continents (Fig.
89 1a and Fig. S1). In line with the surge of B.1.1.7, the N501Y mutation in spike, which is one
90 of the B.1.1.7-defining mutations, has emerged as the most predominant spike mutation since
91 late 2020 (Fig. 1b). This is associated with critical public health importance since N501Y has
92 been implicated in an increased recognition of mouse ACE2¹⁸, hinting that the naturally-
93 emerging N501Y-carrying SARS-CoV-2 variants, including B.1.1.7, B.1.351, P.1, and P.3,
94 may have evolved to infect rodents. To evaluate this possibility, we assessed SARS-CoV-2
95 pseudovirus entry in the non-permissive BHK21 cells with mouse ACE2 (mACE2), rat
96 ACE2 (rACE2), or human ACE2 (hACE2) overexpression. Our results demonstrated that
97 BHK21 cells with mACE2 or rACE2 overexpression were permissive to the entry of SARS-
98 CoV-2-N501Y-spike pseudoviruses, but not SARS-CoV-2-WT-spike pseudoviruses. In
99 contrast, both pseudoviruses efficiently utilized hACE2 for entry (Fig. 1c). Next, we
100 evaluated the capacity of SARS-CoV-2 variants to infect BHK21 cells expressing mACE2,

101 rACE2, or hACE2. As demonstrated in Figure 1d and 1e, SARS-CoV-2 WT and B.1 (Fig.
102 S2), which do not carry N501Y, did not infect or replicate in BHK21 cells overexpressing
103 mACE2 or rACE2. In stark contrast, B.1.1.7 and P.3 (Fig. S2), which carry N501Y, both
104 efficiently infected and replicated in mACE2- or rACE2-expressing BHK21 cells (Fig. 1d,e).
105 The viral gene copies in the cell lysate samples of B.1.1.7-infected BHK21 cells expressing
106 mACE2 or rACE2 were 1880 (P=0.0040) and 1623 (P=0.0093) folds higher than that of the
107 control (vector-transfected) BHK21 cells, respectively (Fig. 1e). Together, these findings
108 suggest that the recently emerged N501Y-carrying SARS-CoV-2 variants, including B.1.1.7,
109 B.1.351, P.1, and P.3, can utilize murine ACE2 as entry receptor and may infect murine
110 species without the need of further adaptation.

111

112 To directly address the question of whether these emerging SARS-CoV-2 variants have
113 evolved to gain the capacity to cross species barrier to murine species, we intranasally
114 challenged 6- to 8-week-old C57B6 mice (*Mus musculus*) with B.1.1.7 or WT SARS-CoV-2
115 and collected tissues for virological and histological assessment on 2, 4, and 7 days post
116 infection (d.p.i.) (Fig. 1f). Importantly, in B.1.1.7-inoculated mice, virus gene copies were
117 detected in brain, nasal turbinate, lung, spleen, and colon tissues. In particular, robust virus
118 replication was detected in the nasal turbinate and lung tissues, which were 4044 and 330
119 folds higher than that of WT SARS-CoV-2-inoculated mice at 2 d.p.i., respectively. Viral
120 gene copies were cleared from WT SARS-CoV-2-inoculated mice at 7 d.p.i., but remained
121 readily detectable from the nasal turbinate and lung of B.1.1.7-inoculated mice (Fig. 1g,h).
122 Permissibility to mouse cells was not due to the D614G mutation since B.1 that carries
123 D614G did not infect and replicate in the nasal turbinate and lung of the inoculated mice (Fig.
124 1i). Importantly, high-titer infectious virus particles were recovered from the nasal turbinate
125 and lung of B.1.1.7-inoculated mice at 2 d.p.i. and remained detectable in some of the

126 inoculated animals at 4 d.p.i. and 7 d.p.i (Fig. 1j,k). In comparison, infectious viral titers were
127 only marginally detected in the nasal turbinates of mice inoculated with WT SARS-CoV-2 at
128 2 d.p.i. but not at 4 d.p.i. and 7 d.p.i.. No infectious virus particle could be recovered from the
129 lung of WT SARS-CoV-2-inoculated mice. Together, these findings indicate that the
130 predominant circulating SARS-CoV-2 variant, B.1.1.7, but not WT SARS-CoV-2, can infect
131 mice with robust virus shedding from the nasal turbinate.

132

133 **Mice (*Mus musculus*) develop pathological changes after primary B.1.1.7 inoculation**

134 Next, we evaluated viral antigen expression and virus-induced pathology in the respiratory
135 tract of mice upon B.1.1.7 or WT SARS-CoV-2 inoculation. As demonstrated in Figure 2a,
136 abundant viral nucleocapsid (N) protein expression was detected in mice inoculated with
137 B.1.1.7 but not WT SARS-CoV-2. In the nasal turbinate, robust viral N protein expression
138 was detected in the epithelial lining at 2 d.p.i. (Fig. 2a) and remained detectable at 4 d.p.i.
139 (Fig. S3). In the lung, abundant N protein was detected in the bronchioles and alveoli (Fig.
140 2b). Viral N protein in the lung of B.1.1.7-inoculated mice was most readily detected at 2
141 d.p.i. and remained detectable at 7 d.p.i. (Fig. S3). In contrast to B.1.1.7-inoculated mice, no
142 viral N protein could be detected in the nasal turbinate and lung of WT SARS-CoV-2-
143 inoculated mice (Fig. 2a,b and Fig. S3). Histological examination of B.1.1.7-inoculated mice
144 showed epithelial damage with secretion and cell debris in the nasal turbinate (Fig. 2c, 2
145 d.p.i., red arrows) at 2 d.p.i.. At 4 d.p.i., more severe submucosal infiltration and loss of
146 epithelial integrity were observed in multiple locations (Fig. 2c, 4 d.p.i., red arrows). At 7
147 d.p.i., intact nasal turbinate epithelium with resolved inflammatory infiltration was observed
148 in the B.1.1.7-inoculated mice, indicating regeneration of the epithelial lining after virus
149 infection (Fig. 2c, 7 d.p.i., red arrow). In mice inoculated with WT SARS-CoV-2, the nasal
150 turbinate epithelium remained intact from 2 d.p.i. to 7 d.p.i. (Fig. 2c, blue arrows). In line

151 with the histopathological findings of the nasal turbinate, the lung of B.1.1.7-inoculated mice
152 showed alveolar wall congestion and inflammatory infiltration (Fig. 2d, 2 d.p.i, red arrows)
153 accompanied by alveolar haemorrhage (Fig. 2d, 4 d.p.i, red arrows). Perivascular infiltration
154 and alveolar septal thickening in the lung of B.1.1.7-inoculated mice remained evident at 7
155 d.p.i (Fig. 2d, 7 d.p.i, red arrows). In contrast, the lung of WT SARS-CoV-2-inoculated mice
156 showed no histopathological changes at all examined time points (Fig. 2d, blue arrows).
157 Despite the histopathological changes found in B.1.1.7-inoculated mice, no significant body
158 weight loss was observed (Fig. S4).

159

160 Moreover, we rechallenged B.1.1.7- or WT SARS-CoV-2-inoculated mice at 14 d.p.i. with
161 B.1.1.7 and harvested their nasal turbinate, lung, and blood samples at 14 days post
162 rechallenge (d.p.r.). Our results showed that mice previously inoculated with B.1.1.7 but not
163 WT SARS-CoV-2 were partially protected from virus rechallenge as evidenced by the lower
164 virus gene copy detected in the nasal turbinate and lung (Fig. 2f). In agreement with the
165 observed partial protection, we detected the presence of serum SARS-CoV-2-specific
166 neutralizing antibodies at 14 days post primary virus challenge in B.1.1.7-inoculated but not
167 WT SARS-CoV-2-inoculated mice (Fig. 2g). The level of neutralizing antibody was further
168 enhanced upon rechallenge, in a virus inoculum-dependent manner (Fig. 2h). Taken together,
169 our results demonstrate that the current predominant circulating B.1.1.7 variant has expanded
170 species tropism to mice with high infectious virus titer shedding from their nasal turbinate.

171

172 **B.1.1.7 infects and causes pathological damages in rats (*Rattus norvegicus*)**

173 Brown rats or street rats live in close proximity to humans and play key roles in
174 disseminating zoonotic diseases. Rat ACE2 (rACE2) is similar to mACE2 in amino acid
175 sequences (Fig. S5) and supported B.1.1.7 entry *in vitro* (Fig. 1c-e). To evaluate whether rats

176 are susceptible to B.1.1.7 infection, we challenged 6-week-old Sprague Dawley rats (*Rattus*
177 *norvegicus*) intranasally with B.1.1.7 or WT SARS-CoV-2 (Fig. 3a). Similar to B.1.1.7
178 infection in mice, the viral gene copies of the inoculated rats peaked at 2 d.p.i. and were 17.0-
179 and 1,831.7-folds higher in the nasal turbinate and lung, respectively, than that of WT SARS-
180 CoV-2-inoculated rats (Fig. 3b,c). Importantly, infectious virus titers were recovered from the
181 nasal turbinate and lung of B.1.1.7-inoculated but not WT SARS-CoV-2-inoculated rats,
182 indicating that rats were permissive to B.1.1.7 but not WT SARS-CoV-2 (Fig. d,e). In line
183 with the infectious virus titer results, immunohistochemistry staining revealed that viral N
184 protein was more frequently detected in the lung than the nasal turbinate of B.1.1.7-
185 inoculated rats (Fig. 3f), while viral N protein was absent in the lung and nasal turbinate of
186 WT SARS-CoV-2-inoculated rats (Fig. 3f).

187

188 In the nasal turbinate of B.1.1.7-inoculated rats, histological examination showed loss of
189 mucosal integrity and epithelial damage at 2 d.p.i. (Fig. 3g, 2 d.p.i., red arrows). More severe
190 epithelial sloughing and submucosal infiltration were detected at 4 d.p.i. (Fig. 3g, 4 d.p.i., red
191 arrow), which were largely regenerated at 7 d.p.i. (Fig. 3g, 7 d.p.i., red arrow). In contrast,
192 the epithelial lining in the nasal turbinate of WT SARS-CoV-2-inoculated rats remained
193 intact at all time points examined (Fig. 3g, blue arrows). In the lung of B.1.1.7-inoculated
194 rats, moderate to severe multi-focal consolidation in the alveoli was observed at 2 d.p.i. (Fig.
195 3h, 2 d.p.i., red arrows). Moreover, necrotic cell debris in the bronchioles, perivascular
196 cuffing caused by inflammatory infiltration, fibrin deposition in the interstitium, and alveolar
197 septa thickening were also observed (Fig. 3i). Alveolar congestion, epithelial disruption in the
198 bronchioles, and alveoli infiltration remained evident at 4 d.p.i. (Fig. 3h, 4 d.p.i., red arrows).
199 Upon viral clearance at 7 d.p.i., these lung pathologies were largely resolved (Fig. 3h, 7 d.p.i.,
200 red arrows). In contrast to B.1.1.7-inoculated rats, no pathological change was observed in

201 the lung of WT SARS-CoV-2-inoculated rats at any examined time points (Fig. 3h, blue
202 arrows). These findings reveal that the current predominant circulating SARS-CoV-2 variant,
203 B.1.1.7, has evolved to expand species tropism beyond WT SARS-CoV-2, and can infect
204 rodents including rats and mice.

205

206 **Differential SARS-CoV-2 tropism in K18-hACE2 and wild type mice**

207 Since mice are not susceptible to WT SARS-CoV-2 infection ¹², the K18-hACE2 transgenic
208 mice are utilized as an animal model for SARS-CoV-2 infection ¹⁹. Our current findings
209 reveal that B.1.1.7 can naturally infect mice, which may serve as a new animal model for
210 SARS-CoV-2 infection that does not require prior virus adaptation or introduction of human
211 ACE2 to the mice. To compare the two infection models, we first characterized the
212 physiological distribution of ACE2 in the two mouse models (Fig. 4a). Our data showed that
213 the K18-hACE2 and C57B6 mice expressed comparable levels of mACE2. Mouse ACE2
214 expression in the intestine was the highest, followed by kidney, colon, lung, and nasal
215 turbinate (Fig. 4b), which resembled the natural ACE2 distribution in human ^{20,21}. In addition
216 to mACE2, K18-hACE2 mice express high level of hACE2 at all evaluated organs (Fig. 4c).
217 The hACE2 expression level was 3,719.1-, 28.3-, 1.1-, 369.2-, 8,285.5-, 1,035.8-, 26.0-, 37.1-
218 , and 36.0-folds higher than that of the mACE2 expression in brain, nasal turbinate, lung,
219 heart, liver, spleen, small intestine, colon, and kidney of K18-hACE2 mice, respectively (Fig.
220 4b,c).

221

222 Next, we in parallel inoculated 6- to 8-week-old C57B6 and K18-hACE2 mice with B.1.1.7
223 and evaluated virus replication at 2 d.p.i.. Interestingly, our results indicated that B.1.1.7
224 replication was more robust in the nasal turbinate of C57B6 mice than that of the K18-
225 hACE2 mice [(vRNA; C57B6: 2.15×10^6 vs K18-hACE2: 2.17×10^4 ; $p=0.0234$) and (PFU;

226 C57B6: 9.87×10^5 vs K18-hACE2: 1.50×10^5 ; $p=0.0014$]. In contrast, B.1.1.7 replication was
227 more robust in the lungs of K18-hACE2 mice than that of the C57B6 mice [(vRNA; C57B6:
228 $1.08 \times 10^4/10^3$ HPRT vs K18-hACE2: $5.36 \times 10^6/10^3$ HPRT; $p=0.0005$) and (PFU; C57B6:
229 7.67×10^4 /gram tissue vs K18-hACE2: 1.02×10^7 /gram tissue; $p<0.0001$] (Fig. 4d,e). These
230 findings were validated by immunohistochemistry staining, which consistently detected more
231 abundant viral N protein expression in the nasal turbinate of C57B6 mice than K18-ACE2
232 mice. Similarly, viral N protein was most frequently and abundantly detected in the lung of
233 K18-hACE2 mice than C57B6 mice (Fig. 4f). In addition to the nasal turbinate and lung, high
234 levels of infectious virus titer and viral antigen expression were detected in the brain of K18-
235 hACE2 mice, which is suggested to cause fatal outcome in the infected animals ²². In
236 contrast, the brain of C57B6 mice was free of either infectious virus particles or viral antigen
237 expression (Fig. 4e,f). In addition to evaluating B.1.1.7 infection in C57B6 and K18-hACE2
238 mice, we additionally compared the infection of B.1.1.7 and WT SARS-CoV-2 in K18-
239 hACE2 mice. Our results indicated that the B.1.1.7 and WT SARS-CoV-2 have similar
240 replication efficiency in the nasal turbinate and lung of K18-hACE2 mice (Fig. S6). Taken
241 together, the B.1.1.7-inoculated C57B6 mouse model may represent a more physiologically
242 relevant model for studying SARS-CoV-2 pathogenesis and therapeutics evaluation due to its
243 native ACE2 distribution profile, while the K18-hACE2 mouse model will be useful for
244 studying the central nervous system pathologies of SARS-CoV-2 infection.

245

246 **Discussion**

247 In summary, we demonstrate that the current dominant circulating SARS-CoV-2 variant,
248 B.1.1.7, has evolved to gain the capability to cross species barrier to infect rodents including
249 mice and rats, which are not permissive to WT SARS-CoV-2. Mice and rats reside in close
250 proximity to humans, including densely populated areas with circulating B.1.1.7 and/or other

251 N501Y-carrying SARS-CoV-2 variants. The acquired susceptibility of these rodents to
252 SARS-CoV-2 variants has substantially increased the risk of SARS-CoV-2 infection in the
253 rodent population, which may result in a zoonotic reservoir of SARS-CoV-2. In particular,
254 our results indicate that B.1.1.7-infected mice and rats can shed infectious virus particles in
255 the respiratory tract for approximately 4 to 7 days after infection, which may contaminate the
256 environment and become a persistent source of human infection. Importantly, SARS-CoV-2
257 adaptation in mice occurs rapidly, with mouse-adapting mutations usually developing within
258 1-to-10 passages^{18,23-25}. These mutations will result in even more robust SARS-CoV-2
259 replication in rodents and may further facilitate virus dissemination.

260

261 Interspecies spill-over of SARS-CoV-2 is not uncommon. While SARS-CoV-2 is presumed
262 to have originated from an animal reservoir, humans are also known to infect other animals
263 with SARS-CoV-2, including cats, dogs, and even tigers in zoos²⁶⁻²⁸. A previous study
264 demonstrated that bidirectional SARS-CoV-2 transmission could occur between humans and
265 minks²⁹. Rodents including mice and rats were previously not permissive to SARS-CoV-2
266 infection and were thus not considered to be an important animal reservoir of the ongoing
267 COVID-19 pandemic. However, as demonstrated in the current study, the evolving SARS-
268 CoV-2 variants with the N501Y mutation in spike can now naturally infect mice and rats, and
269 potentially other rodent species. Considering the abundance of these animals and their
270 proximate habitats with humans, humans-to-rodents and rodents-to-humans transmissions
271 may be inevitable. Public health measures including stringent rodent control and surveillance
272 on SARS-CoV-2 infection in the rodent populations especially in densely populated regions
273 should be implemented to facilitate the control of the pandemic.

274

275 **Methods**

276 **Viruses and biosafety**

277 All virus strains used in this study were shown in Figure S2. SARS-CoV-2 wildtype virus
278 HKU-001a (GenBank: MT230904) was a clinical isolate as previously described¹¹. SARS-
279 CoV-2 B.1 (GISAID: EPI_ISL_497840), B.1.1.7 (GISAID: EPI_ISL_1273444), and
280 B.1.1.28.3 (P.3) (GISAID: EPI_ISL_1660475) were isolated from laboratory-confirmed
281 COVID-19 patients in Hong Kong. *In vitro* and *in vivo* experiments involving infectious wild
282 type SARS-CoV-2, B.1, B.1.1.7, and P.3 were performed in Biosafety Level 3 laboratory and
283 strictly followed the approved standard operation procedures.

284

285 **SARS-CoV-2-Spike-pseudovirus entry assay**

286 The SARS-CoV-2-WT-S and SARS-CoV-2-N501Y-S pseudoviruses were generated in 293T
287 cells as we previously described³⁰. For pseudovirus entry assays, mouse ACE2, rat ACE2, or
288 human ACE2 were transfected into BHK21 cells. At 24-hour post transfection, transfected
289 cells were inoculated with pseudoviruses for 24 h before washed and lysed for measuring
290 luciferase activity with a firefly luciferase assay system (E1501, Promega).

291

292 ***In vivo* virus challenge**

293 The use of animals was approved by the Committee on the Use of Live Animals in Teaching
294 and Research of The University of Hong Kong. Heterogenous K18-hACE2 C57BL/6J mice
295 (2B6.Cg-Tg(K18-ACE2)2Prln/J) were obtained from The Jackson Laboratory. For virus
296 challenge in mice, 6- to 8- week-old female C57BL/6J mice or K18-hACE2 transgenic mice
297 were anaesthetized with ketamine and xylazine, followed by intranasal inoculation with 20
298 μ l/mouse of WT, B.1, or B.1.1.7 SARS-CoV-2 at 4×10^3 PFU/mouse as we previously
299 described³¹. For SARS-CoV-2 infection in rats, 6-week-old female Sprague Dawley rats
300 were anaesthetized with ketamine and xylazine, followed by intranasal inoculation with

301 4×10⁵ PFU/rat of WT or B.1.1.7 SARS-CoV-2 diluted in 50µl PBS. On day 2-, 4- and 7-day
302 post virus challenge, animals were euthanized for harvesting organs for viral load titration
303 and histology staining.

304

305 **RNA extraction and quantitative RT-PCR**

306 RNA extraction and RT-qPCR were performed as we previously described ¹¹. SARS-CoV-2
307 genome copies were quantified with sequence-specific probe and primers targeting the RNA-
308 dependent RNA polymerase ¹¹.

309

310 **Infectious virus titration by plaque assays**

311 Organs harvested from virus-inoculated animals were homogenized in DMEM with Tissue
312 Lyzer II, followed by centrifugation and titration. To titrate the infectious virus titer, tissue
313 homogenates were 10-fold serially-diluted with DMEM and applied to monolayered VeroE6
314 cells for 2h. After inoculation, cells were washed once before overlaid with 1% low-melting
315 agarose containing 1% FBS. Cells were further incubated for 72 h and fixed with 0.5%
316 crystal violet for visualizing plaque formation ³².

317

318 **Histology and immunohistochemistry staining**

319 Animal tissues were harvested and fixed with 10% neutral-buffered formalin. Nasal
320 turbinates were decalcified with 10% formic acid for 7 days before being processed with the
321 TP1020 Leica semi-enclosed benchtop tissue processor. IHC was performed with the DAB
322 (3,3'-diaminobenzidine) substrate kit (Vector Laboratories) as we previously described ³³. To
323 detect the viral antigen, in-house mouse monoclonal biotinylated anti-SARS-CoV-2
324 nucleocapsid protein antibody was used, followed by color development with the DAB
325 substrate kit. The nuclei were detected with haematoxylin before the tissue sections was

326 mounted with the VectaMount permanent mounting medium (Vector Laboratories). For H&E
327 staining, tissue sections were stained with Gill's haematoxylin and eosin-Y. Images were
328 acquired with the Olympus BX53 light microscope.

329

330 **Immunofluorescence staining**

331 Nucleocapsid of SARS-CoV-2 was detected by the in-house rabbit polyclonal anti-SARS-
332 CoV-2 nucleocapsid antibody as we previously reported ³⁴. Nuclei were stained with the
333 DAPI dye (Thermo Fisher Scientific) before the tissue sections being mounted with the
334 Diamond Prolong Antifade mounting buffer (Thermo Fisher Scientific). Images were
335 acquired with the Olympus BX53 light microscope.

336

337 **Neutralizing antibody assay**

338 Mice serum was obtained immediately before virus rechallenge and 14 days post rechallenge.
339 Sera were heat-inactivated for 30 m at 56 °C before use. Two-fold serially diluted sera was
340 incubated with 100 TCID₅₀ WT SARS-CoV-2 for 1 h at 37 °C. After incubation, the virus-
341 sera mixture was inoculated in VeroE6 cells and further incubated for 72 h for cytopathic
342 effect (CPE) development. The neutralization titer was determined by observing the highest
343 dilution without CPE.

344

345 **Multiple sequence alignment and docking**

346 Sequence alignment and docking were performed as we previously described ³⁵. ACE2
347 protein sequences of human (Q9BYF1), mouse (Q8R0I0), and rat (Q5EGZ1) were retrieved
348 from Uniprot. Multiple sequence alignment was constructed with Muscle. The crystal
349 structure of wildtype SARS-CoV-2 spike RBD and human ACE2 complex (code: 6M0J) was
350 retrieved from the Protein Data Bank. Mouse and rat ACE2 structures were generated by

351 mutating the interface residues within 4.0Å of RBD according to the multiple sequence
352 alignment. The complex of ACE2 and N501Y RBD was built by superimposition of N501Y
353 RBD (code: 7NEG) with wildtype RBD. All ACE2-RBD complexes were relaxed and locally
354 refined with Rosetta Relax and Docking protocols. Interface binding energies were estimated
355 with InterfaceAnalyzer application.

356

357 **Statistical analysis**

358 Data analysis were performed with Graphpad prism 8.0. Statistical comparison between
359 different groups was performed by one-way ANOVA, two-way ANOVA, or Student's t-test.
360 Differences were considered statistically significant when $p < 0.05$.

361

362 **Acknowledgments**

363 This work was partly supported by the donations of the Shaw Foundation of Hong Kong, the
364 Richard Yu and Carol Yu, Michael Seak-Kan Tong, May Tam Mak Mei Yin, Lee Wan
365 Keung Charity Foundation Limited, Hong Kong Sanatorium & Hospital, Hui Ming, Hui Hoy
366 and Chow Sin Lan Charity Fund Limited, Chan Yin Chuen Memorial Charitable Foundation,
367 Marina Man-Wai Lee, the Hong Kong Hainan Commercial Association South China
368 Microbiology Research Fund, the Jessie & George Ho Charitable Foundation, Perfect Shape
369 Medical Limited, Kai Chong Tong, Tse Kam Ming Laurence, Foo Oi Foundation Limited,
370 Betty Hing-Chu Lee, Ping Cham So, and Lo Ying Shek Chi Wai Foundation; Funding from
371 the Hong Kong Health and Medical Research Fund (CID-HKU1-5) of the Food and Health
372 Bureau, Hong Kong Special Administrative Region Government; Innovation and Technology
373 Fund (ITF), the Government of the Hong Kong Special Administrative Region; The
374 Consultancy Service for Enhancing Laboratory Surveillance of Emerging Infectious Diseases
375 and Research Capability on Antimicrobial Resistance for Department of Health of the Hong

376 Kong Special Administrative Region Government; The National Program on Key Research
377 Project of China (grant no. 2020YFA0707500 and 2020YFA0707504); Sanming Project of
378 Medicine in Shenzhen, China (SZSM201911014); and the High Level-Hospital Program,
379 Health Commission of Guangdong Province, China. The funding sources had no role in the
380 study design, data collection, analysis, interpretation, or writing of the report.

381

382 **Author contributions**

383 HS, JF-WC, K-YY, and HC had roles in the study design, data collection, data analysis, data
384 interpretation, and writing of the manuscript. TT-TY, CY, JCH, LW, BH, DY, YW, YH, XH,
385 YC, CC-SC, VK-MP, R-QZ, W-MC, JDI, AW-HC, -YFH, J-PC, K-HC, JZ, SS, B-ZZ, SY,
386 AJZ, J-DH, and KK-WT had roles in the experiments, data collection, data analysis, and data
387 interpretation. All authors reviewed and approved the final version of the manuscript.

388

389 **Competing interests**

390 Authors declare that they have no competing interests.

391

392 **Materials and correspondence**

393 Correspondence and material requests should be addressed to Dr. Hin Chu, Prof Kwok-Yung
394 Yuen, or Dr. Jasper Fuk-Woo Chan.

395

396 **Data availability**

397 The data that support the findings of this study are available from the corresponding authors
398 upon reasonable request.

399

400

401 **References**

- 402 1 Chan, J. F., To, K. K., Tse, H., Jin, D. Y. & Yuen, K. Y. Interspecies transmission and emergence of
403 novel viruses: lessons from bats and birds. *Trends Microbiol* **21**, 544-555,
404 doi:10.1016/j.tim.2013.05.005 (2013).
- 405 2 Zhou, P. *et al.* A pneumonia outbreak associated with a new coronavirus of probable bat origin. *Nature*
406 **579**, 270-273, doi:10.1038/s41586-020-2012-7 (2020).
- 407 3 Chan, J. F. *et al.* A familial cluster of pneumonia associated with the 2019 novel coronavirus indicating
408 person-to-person transmission: a study of a family cluster. *Lancet* **395**, 514-523, doi:10.1016/S0140-
409 6736(20)30154-9 (2020).
- 410 4 WHO. (2021).
- 411 5 Hoffmann, M. *et al.* SARS-CoV-2 Cell Entry Depends on ACE2 and TMPRSS2 and Is Blocked by a
412 Clinically Proven Protease Inhibitor. *Cell* **181**, 271-280 e278, doi:10.1016/j.cell.2020.02.052 (2020).
- 413 6 Leung, K., Shum, M. H., Leung, G. M., Lam, T. T. & Wu, J. T. Early transmissibility assessment of the
414 N501Y mutant strains of SARS-CoV-2 in the United Kingdom, October to November 2020. *Euro*
415 *Surveill* **26**, doi:10.2807/1560-7917.ES.2020.26.1.2002106 (2021).
- 416 7 Lau, S. K. *et al.* Discovery of a novel coronavirus, China Rattus coronavirus HKU24, from Norway
417 rats supports the murine origin of Betacoronavirus 1 and has implications for the ancestor of
418 Betacoronavirus lineage A. *J Virol* **89**, 3076-3092, doi:10.1128/JVI.02420-14 (2015).
- 419 8 Firth, C. *et al.* Detection of zoonotic pathogens and characterization of novel viruses carried by
420 commensal *Rattus norvegicus* in New York City. *mBio* **5**, e01933-01914, doi:10.1128/mBio.01933-14
421 (2014).
- 422 9 McFarlane, R., Sleight, A. & McMichael, T. Synanthropy of wild mammals as a determinant of
423 emerging infectious diseases in the Asian-Australasian region. *Ecohealth* **9**, 24-35,
424 doi:10.1007/s10393-012-0763-9 (2012).
- 425 10 Sridhar, S. *et al.* Transmission of Rat Hepatitis E Virus Infection to Humans in Hong Kong: A Clinical
426 and Epidemiological Analysis. *Hepatology* **73**, 10-22, doi:10.1002/hep.31138 (2021).
- 427 11 Chu, H. *et al.* Comparative tropism, replication kinetics, and cell damage profiling of SARS-CoV-2
428 and SARS-CoV with implications for clinical manifestations, transmissibility, and laboratory studies of
429 COVID-19: an observational study. *Lancet Microbe* **1**, e14-e23, doi:10.1016/S2666-5247(20)30004-5
430 (2020).
- 431 12 Bao, L. *et al.* The pathogenicity of SARS-CoV-2 in hACE2 transgenic mice. *Nature* **583**, 830-833,
432 doi:10.1038/s41586-020-2312-y (2020).
- 433 13 Zhai, X. *et al.* Comparison of Severe Acute Respiratory Syndrome Coronavirus 2 Spike Protein
434 Binding to ACE2 Receptors from Human, Pets, Farm Animals, and Putative Intermediate Hosts. *J*
435 *Virol* **94**, doi:10.1128/JVI.00831-20 (2020).
- 436 14 Zhao, X. *et al.* Broad and Differential Animal Angiotensin-Converting Enzyme 2 Receptor Usage by
437 SARS-CoV-2. *J Virol* **94**, doi:10.1128/JVI.00940-20 (2020).
- 438 15 Houriyah Tegally, E. W., Marta Giovanetti, Arash Iranzadeh, Vagner Fonseca, Jennifer Giandhari,
439 Deelan Doolabh, Sureshnee Pillay, Emmanuel James San, Nokukhanya Msomi, Koleka Mlisana, Anne
440 von Gottberg, Sibongile Walaza, Mushal Allam, Arshad Ismail, Thabo Mohale, Allison J Glass, Susan
441 Engelbrecht, Gert Van Zyl, Wolfgang Preiser, Francesco Petruccione, Alex Sigal, Diana Hardie, Gert
442 Marais, Marvin Hsiao, Stephen Korsman, Mary-Ann Davies, Lynn Tyers, Innocent Mudau, Denis
443 York, Caroline Maslo, Dominique Goedhals, Shareef Abrahams, Oluwakemi Laguda-Akingba,
444 Arghavan Alisoltani-Dehkordi, Adam Godzik, Constantinos Kurt Wibmer, Bryan Trevor Sewell, José
445 Lourenço, Luiz Carlos Junior Alcantara, Sergei L Kosakovsky Pond, Steven Weaver, Darren Martin,
446 Richard J Lessells, Jinal N Bhiman, Carolyn Williamson, Tulio de Oliveira. Emergence and rapid
447 spread of a new severe acute respiratory syndrome-related coronavirus 2 (SARS-CoV-2) lineage with
448 multiple spike mutations in South Africa. *medRxiv*, doi:<https://doi.org/10.1101/2020.12.21.20248640>
449 (2020).
- 450 16 Voloch, C. M. *et al.* Genomic characterization of a novel SARS-CoV-2 lineage from Rio de Janeiro,
451 Brazil. *J Virol*, doi:10.1128/JVI.00119-21 (2021).
- 452 17 Francis A. Tablizo, K. M. K., Carlo M. Lapid, Marc Jerrone R. Castro, Maria Sofia L. Yangzon,
453 Benedict A. Maralit, Marc Edsel C. Ayes, Eva Maria Cutiongeo-de la Paz, Alethea R. De Guzman, Jan
454 Michael C. Yap, Jo-Hannah S. Llamas, Shiela Mae M. Araiza, Kris P. Punayan, Irish Coleen A. Asin,
455 Candice Francheska B. Tambaoan, Asia Louisa U. Chong, Karol Sophia Agape R. Padilla, Rianna
456 Patricia S. Cruz, El King D. Morado, Joshua Gregor A. Dizon, Razel Nikka M. Hao, Arianne A.
457 Zamora, Devon Ray Pacial, Juan Antonio R. Magalang, Marissa Alejandria, Celia Carlos, Anna Ong-
458 Lim, Edsel Maurice Salvaña, John Q. Wong, Jaime C. Montoya, Maria Rosario Singh-Vergeire,
459 Cynthia P. Saloma. Genome sequencing and analysis of an emergent SARS-CoV-2 variant

460 characterized by multiple spike protein mutations detected from the Central Visayas Region of the
461 Philippines. *medRxiv*, doi:<https://doi.org/10.1101/2021.03.03.21252812> (2021).

462 18 Gu, H. *et al.* Adaptation of SARS-CoV-2 in BALB/c mice for testing vaccine efficacy. *Science* **369**,
463 1603-1607, doi:10.1126/science.abc4730 (2020).

464 19 Zheng, J. *et al.* COVID-19 treatments and pathogenesis including anosmia in K18-hACE2 mice.
465 *Nature* **589**, 603-607, doi:10.1038/s41586-020-2943-z (2021).

466 20 Hamming, I. *et al.* Tissue distribution of ACE2 protein, the functional receptor for SARS coronavirus.
467 A first step in understanding SARS pathogenesis. *J Pathol* **203**, 631-637, doi:10.1002/path.1570
468 (2004).

469 21 Hikmet, F. *et al.* The protein expression profile of ACE2 in human tissues. *Mol Syst Biol* **16**, e9610,
470 doi:10.15252/msb.20209610 (2020).

471 22 McCray, P. B., Jr. *et al.* Lethal infection of K18-hACE2 mice infected with severe acute respiratory
472 syndrome coronavirus. *J Virol* **81**, 813-821, doi:10.1128/JVI.02012-06 (2007).

473 23 Zhang, Y. *et al.* SARS-CoV-2 rapidly adapts in aged BALB/c mice and induces typical pneumonia. *J*
474 *Virol*, doi:10.1128/JVI.02477-20 (2021).

475 24 Wang, J. *et al.* Mouse-adapted SARS-CoV-2 replicates efficiently in the upper and lower respiratory
476 tract of BALB/c and C57BL/6J mice. *Protein Cell* **11**, 776-782, doi:10.1007/s13238-020-00767-x
477 (2020).

478 25 Leist, S. R. *et al.* A Mouse-Adapted SARS-CoV-2 Induces Acute Lung Injury and Mortality in
479 Standard Laboratory Mice. *Cell* **183**, 1070-1085 e1012, doi:10.1016/j.cell.2020.09.050 (2020).

480 26 Garigliany, M. *et al.* SARS-CoV-2 Natural Transmission from Human to Cat, Belgium, March 2020.
481 *Emerg Infect Dis* **26**, 3069-3071, doi:10.3201/eid2612.202223 (2020).

482 27 Sit, T. H. C. *et al.* Infection of dogs with SARS-CoV-2. *Nature* **586**, 776-778, doi:10.1038/s41586-
483 020-2334-5 (2020).

484 28 McAloose, D. *et al.* From People to Panthera: Natural SARS-CoV-2 Infection in Tigers and Lions at
485 the Bronx Zoo. *mBio* **11**, doi:10.1128/mBio.02220-20 (2020).

486 29 Oude Munnink, B. B. *et al.* Transmission of SARS-CoV-2 on mink farms between humans and mink
487 and back to humans. *Science* **371**, 172-177, doi:10.1126/science.abe5901 (2021).

488 30 Chu, H. *et al.* Host and viral determinants for efficient SARS-CoV-2 infection of the human lung. *Nat*
489 *Commun* **12**, 134, doi:10.1038/s41467-020-20457-w (2021).

490 31 Chu, H. *et al.* Targeting highly pathogenic coronavirus-induced apoptosis reduces viral pathogenesis
491 and disease severity. *Sci Adv* **7**, doi:10.1126/sciadv.abf8577 (2021).

492 32 Chu, H. *et al.* Comparative Replication and Immune Activation Profiles of SARS-CoV-2 and SARS-
493 CoV in Human Lungs: An Ex Vivo Study With Implications for the Pathogenesis of COVID-19. *Clin*
494 *Infect Dis* **71**, 1400-1409, doi:10.1093/cid/ciaa410 (2020).

495 33 Chu, H. *et al.* SARS-CoV-2 Induces a More Robust Innate Immune Response and Replicates Less
496 Efficiently Than SARS-CoV in the Human Intestines: An Ex Vivo Study With Implications on
497 Pathogenesis of COVID-19. *Cell Mol Gastroenterol Hepatol* **11**, 771-781,
498 doi:10.1016/j.jcmgh.2020.09.017 (2021).

499 34 Shuai, H. *et al.* Differential immune activation profile of SARS-CoV-2 and SARS-CoV infection in
500 human lung and intestinal cells: Implications for treatment with IFN-beta and IFN inducer. *J Infect* **81**,
501 e1-e10, doi:10.1016/j.jinf.2020.07.016 (2020).

502 35 Chan, J. F. *et al.* Simulation of the Clinical and Pathological Manifestations of Coronavirus Disease
503 2019 (COVID-19) in a Golden Syrian Hamster Model: Implications for Disease Pathogenesis and
504 Transmissibility. *Clin Infect Dis* **71**, 2428-2446, doi:10.1093/cid/ciaa325 (2020).

506

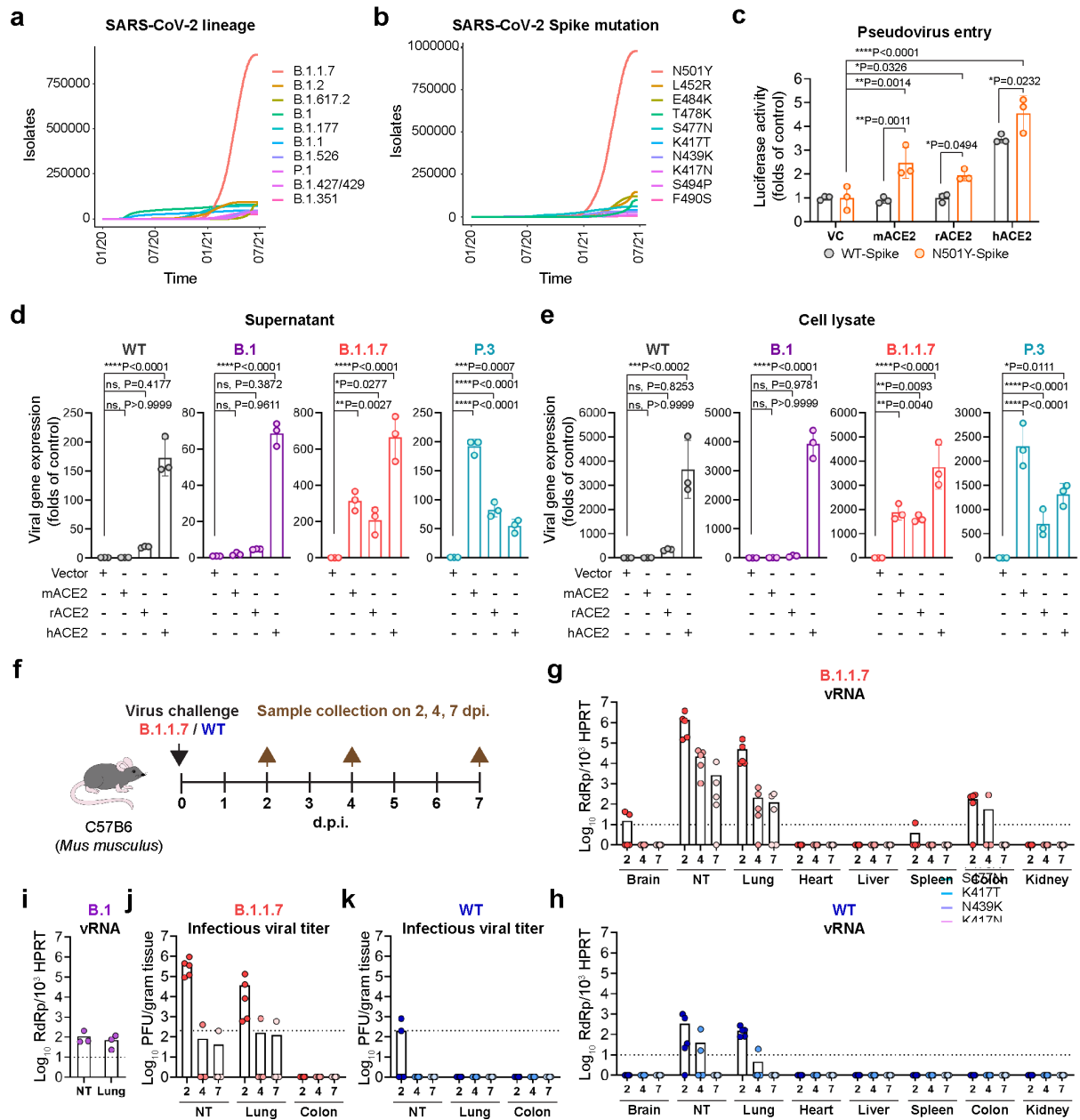
507

508

509

510

511



513

514 **Figure 1. The predominant circulating SARS-CoV-2 variant B.1.1.7 efficiently infects**

515 **mice. (a)** Top 10 prevalent lineages of SARS-CoV-2 and **(b)** Top 10 amino acid mutations in

516 the spike of SARS-CoV-2 variants retrieved from the GISAID EpiCoV database as of June

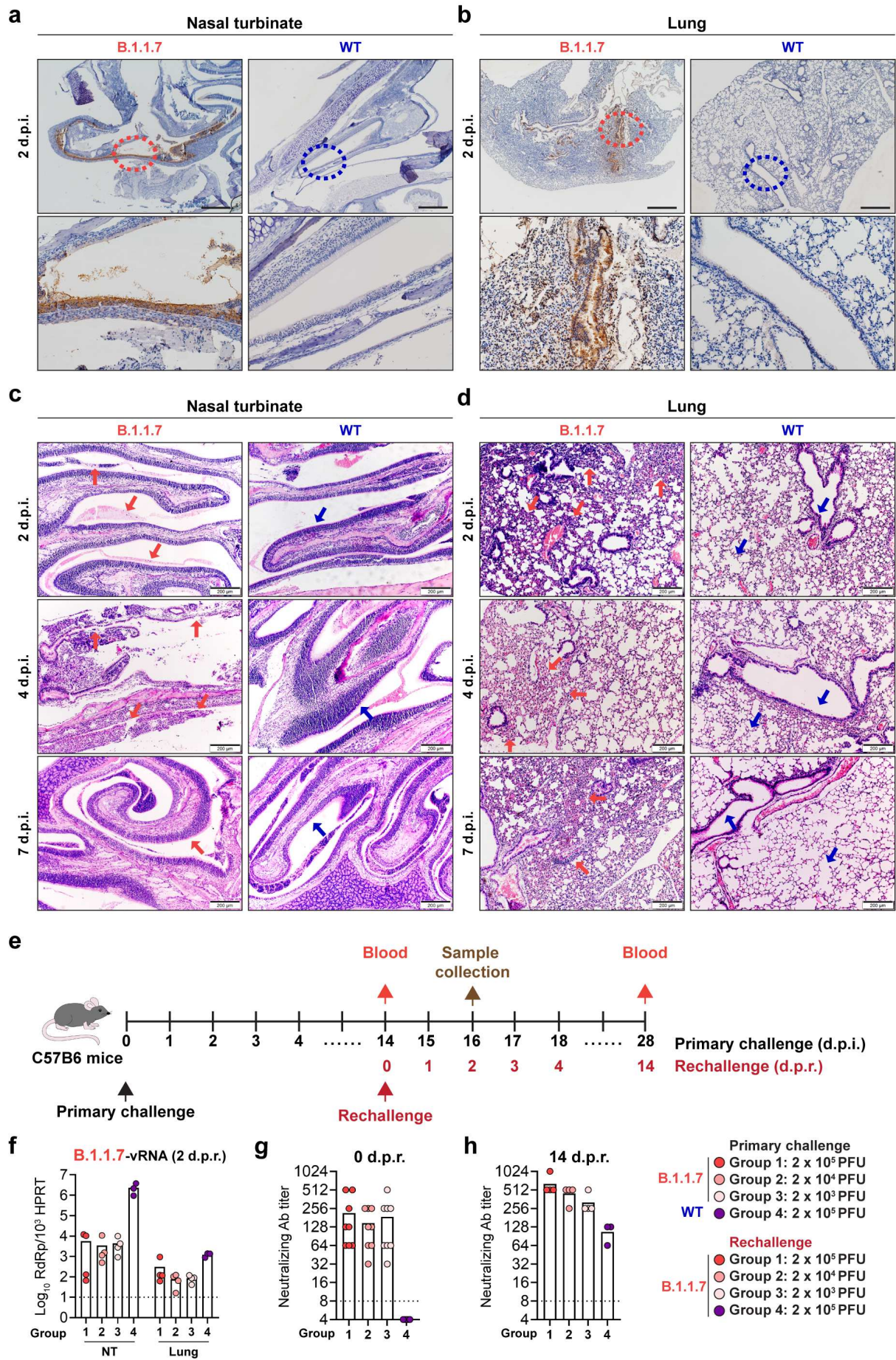
517 28th, 2021. **(c)** BHK21 cells transfected with empty vector, mouse ACE2, rat ACE2 or human

518 ACE2 were inoculated with SARS-CoV-2-S-pseudoviruses with either WT or N501Y spike. Pseudovirus entry

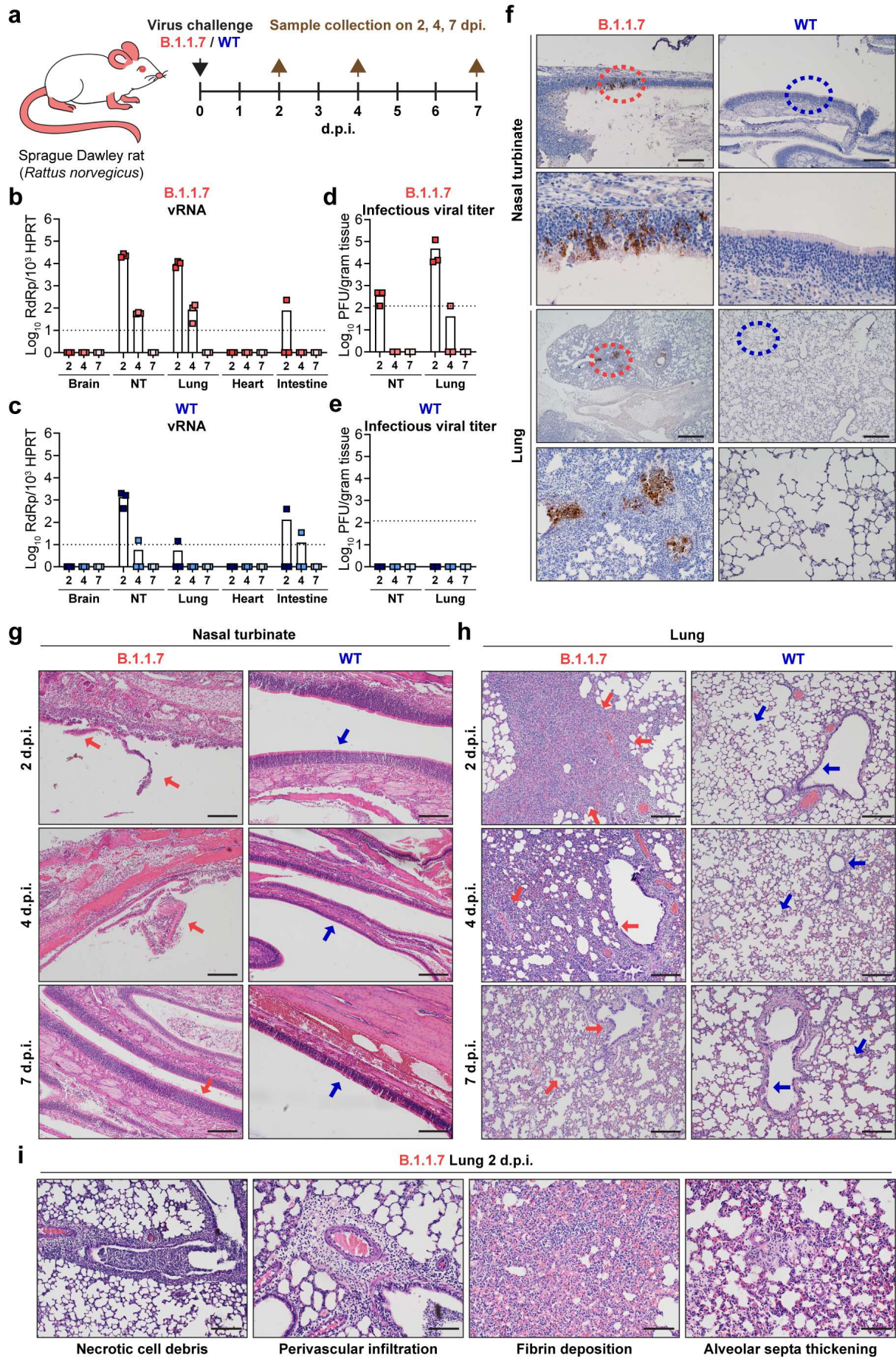
519 was determined at 24h post inoculation ($n = 3$). VC, vector control. **(d and**

520 **e)** BHK21 cells overexpressing empty vector, mouse ACE2, rat ACE2 and human ACE2 were

521 infected with B.1, B.1.1.7, P.3, or WT SARS-CoV-2. Relative viral gene expression in (d)
522 supernatants and (e) cell lysates were determined by RT-qPCR ($n = 3$). (f-k) 6-to-8-week-old
523 C57B6 mice were intranasally inoculated with B.1.1.7, B.1, or WT SARS-CoV-2. Mice were
524 euthanized on 2, 4 or 7 d.p.i. and tissues were harvested for viral titer quantification. (f)
525 Schematic illustration of the *in vivo* infection experiment in C57B6 mice. (g-i) Viral gene
526 copies from mice infected with B.1.1.7, B.1, or WT SARS-CoV-2. (j and k) Infectious viral
527 titer in the nasal turbinates, lungs and colons of mice inoculated with B.1.1.7 or WT SARS-
528 CoV-2. Dashed line indicates detection limits. Data represents mean \pm SD from the indicated
529 number of biological repeats. Statistical differences were determined with two-way analysis
530 of variance (ANOVA) in (c), (d) and (e). * represented $P < 0.05$; ** represented $P < 0.01$;
531 *** represented $P < 0.001$; **** represented $P < 0.0001$. WT, wild type SARS-CoV-2. NT,
532 nasal turbinate.
533

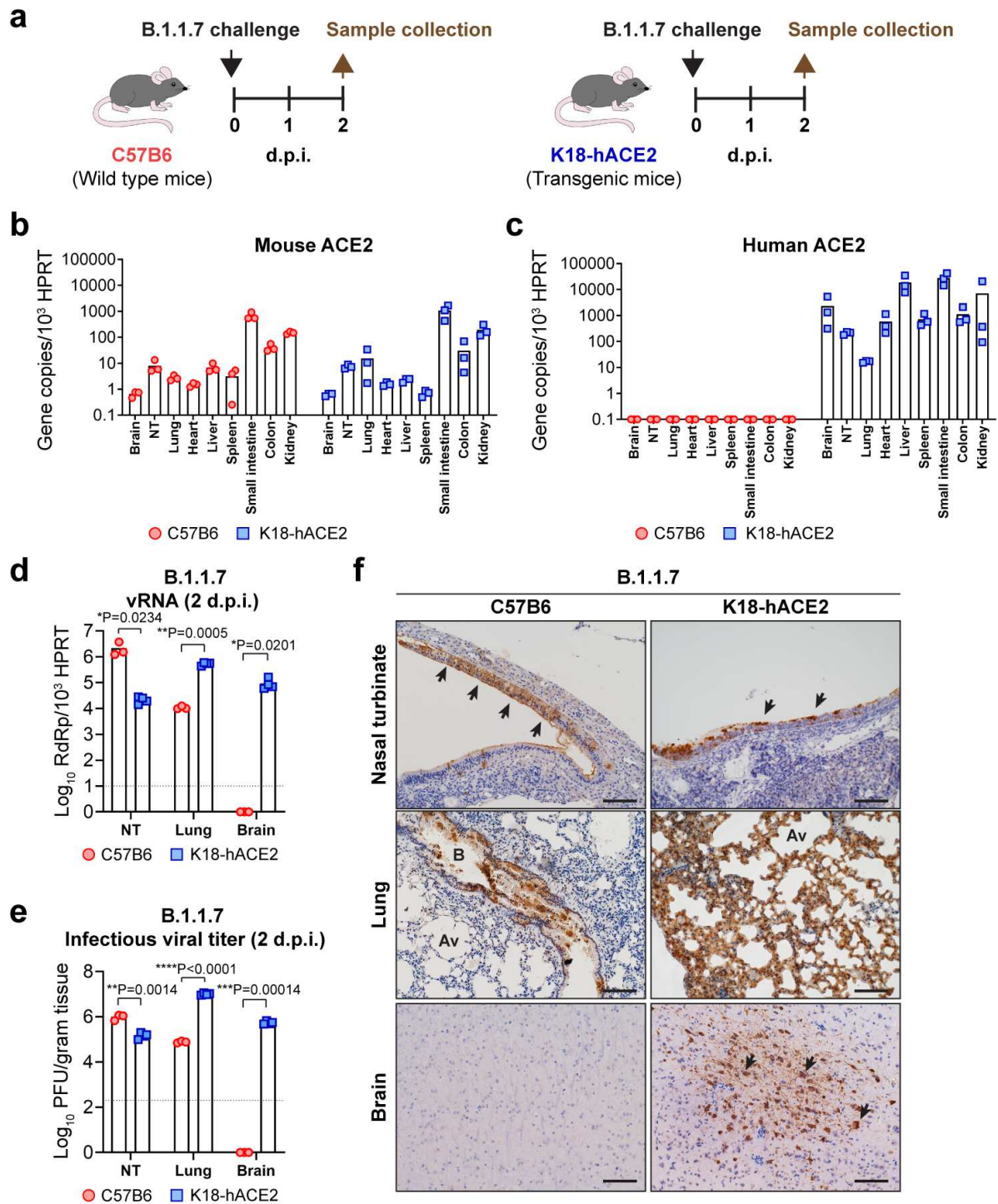


535 **Figure 2. Mice (*Mus musculus*) develop pathological changes after primary B.1.1.7**
536 **inoculation. (a-d)** C57B6 mice intranasally inoculated with B.1.1.7 or WT SARS-CoV-2
537 were euthanized for harvesting nasal turbinate and lung tissues on 2, 4 and 7 d.p.i..
538 Representative images of immunohistochemistry staining for the detection of nucleocapsid
539 protein (brown) in the (a) nasal turbinates and (b) lung on 2 d.p.i.. Insets were shown below
540 for the circled areas. Scale bar, 500 μm . (c) Representative images of hematoxylin and eosin
541 (H&E) staining of mouse nasal turbinates harvested on 2, 4 and 7 d.p.i.. Pathological changes
542 in the B.1.1.7-inoculated mice on 2 d.p.i. and 4 d.p.i. were pointed out with red arrows. On 7
543 d.p.i., the integrity of the nasal cavity epithelium was restored (red arrow). Intact nasal
544 epithelium layers of the WT SARS-CoV-2-inoculated mice were shown for comparison (blue
545 arrows). (d) Representative images of H&E staining of mouse lungs harvested on 2, 4 and 7
546 d.p.i.. In the lungs of B.1.1.7-inoculated mice, alveolar wall congestion and alveolar
547 infiltrations were detected on 2 d.p.i. (red arrows). Alveolar haemorrhage was developed on 4
548 d.p.i. (red arrows). Alveolar septa thickening remained evident on 7 d.p.i.. Normal structure
549 of bronchioles and alveoli in the lung of the WT SARS-CoV-2-inoculated mice were
550 indicated by blue arrows for comparison. Scale bar, 200 μm . **(e-h)** C57B6 mice were
551 intranasally inoculated with 2×10^5 PFU WT SARS-CoV-2 or B.1.1.7 at 2×10^3 , 2×10^4 , or
552 2×10^5 PFU, followed by rechallenge on 14 d.p.i. with B.1.1.7 at the indicated titers. (e)
553 Schematic illustration of the rechallenge experiment. (f) Viral titer in nasal turbinate and lung
554 of the infected mice on day 2 post rechallenge quantified with RT-qPCR ($n = 4$ for group 1-3,
555 $n = 3$ for group 4). (g) Neutralizing antibody titer in mouse sera harvested on 0 day post
556 rechallenge (d.p.r.) ($n = 8$ for group 1-3, $n = 3$ for group 4) and (h) 14 d.p.r. ($n = 4$ for group
557 1-3, $n = 3$ for group 4). Dashed line indicates the detection limit of each assay. NT, nasal
558 turbinate.



560 **Figure 3. B.1.1.7 infects and causes pathological damages in rats (*Rattus norvegicus*). (a)**
561 Schematic illustration of *in vivo* infection experiment in Sprague Dawley rats. 6-week-old
562 Sprague Dawley rats were intranasally inoculated with B.1.1.7 or WT SARS-CoV-2. On 2, 4
563 and 7 d.p.i., rats were euthanized for harvesting tissues for virological assessment and
564 histopathological analysis. (b and c) Viral titer quantified with RT-qPCR in the brain, nasal
565 turbinate, lung, heart and intestine of the inoculated rats. NT, nasal turbinate. (d and e)
566 Infectious viral titer quantified with plaque assays in the nasal turbinate and lung of the
567 inoculated rats. (f) Immunohistochemistry staining for the detection of nucleocapsid protein
568 expression (brown) in the nasal turbinate and lung of the inoculated rats on 2 d.p.i. Insets
569 were shown below for the circled areas. Scale bar, 200 μm for nasal turbinate; 500 μm for
570 lung. (g-i) Histopathological analysis for nasal turbinate and lung harvested on 2, 4, and 7
571 d.p.i.. (g) Representative H&E images showing pathological changes in the nasal cavity of
572 B.1.1.7-inoculated rats, including epithelial damage and loss of mucosal integrity (2 d.p.i., red
573 arrow). On 4 d.p.i., more severe epithelial sloughing and submucosal infiltrations were
574 detected (4 d.p.i., red arrow). On 7 d.p.i., the epithelial lining was largely restored (7 d.p.i.,
575 red arrow). In contrast, the structure of the nasal turbinate in WT SARS-CoV-2-inoculated
576 rats remained undisrupted throughout the course of experiment. (h) Representative H&E
577 images showing severe alveoli consolidation (2 d.p.i., red arrows), epithelium disruption and
578 alveoli infiltrations (4 d.p.i., red arrows) in the lungs of B.1.1.7-inoculated rats. Acute lung
579 injuries were largely repaired by 7 d.p.i. and normal structure of the alveoli and lung were
580 indicated by red arrows. No pathological change was observed in either alveoli or
581 bronchioles of WT SARS-CoV-2-inoculated rats (2, 4, and 7 d.p.i., blue arrows). Scale bar,
582 200 μm . (i) Typical pulmonary lesions detected in the lungs of B.1.1.7-inoculated rats on 2
583 d.p.i.. Scale bar, 100 μm .

584



585

586 **Figure 4. Differential SARS-CoV-2 tropism in K18-hACE2 and wild type mice. (a)**

587 Schematic illustration of comparative study of SARS-CoV-2 B.1.1.7 tropism in C57B6 and

588 K18-hACE2 mice. **(b)** Mouse ACE2 expression quantified with RT-qPCR. **(c)** Human ACE2

589 expression quantified with RT-qPCR. **(d)** Viral gene copy in nasal turbinate, lung and brain

590 of the B.1.1.7-inoculated C57B6 and K18-hACE2 mice quantified with RT-qPCR. **(e)**

591 Infectious viral titers in nasal turbinate, lung, and brain of B.1.1.7-inoculated C57B6 and
592 K18-hACE2 mice quantified with plaque assays. (f) Representative immunohistochemistry
593 images of nasal turbinate, lung, and brain of B.1.1.7-inoculated C57B6 and K18-hACE2
594 mice. Presence of SARS-CoV-2 nucleocapsid protein were shown in brown and indicated by
595 black arrows. Scale bar, 100 μ m. Statistical differences were determined with two-tailed
596 Student's *t*-test in (d) and (e). * represented $P < 0.05$; ** represented $P < 0.01$; ***
597 represented $P < 0.001$; **** represented $P < 0.0001$. Av, alveoli; B, bronchioles. NT, nasal
598 turbinates; SI, small intestine.

599

600

601

602

603

604

605

606

607

608

609

610

611

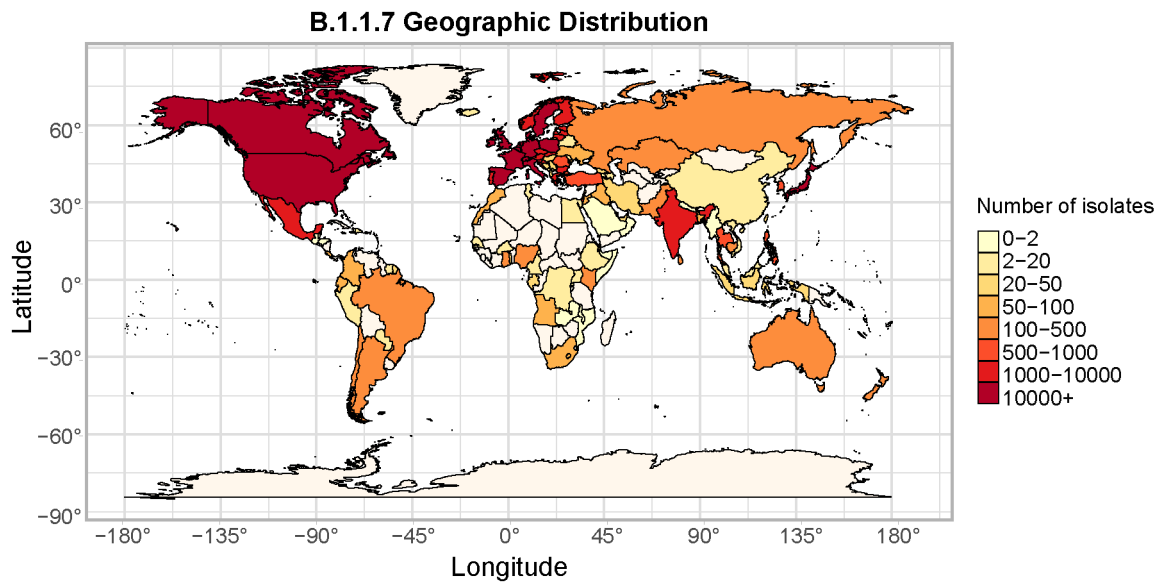
612

613

614

615

616 **Supplementary figures and supplementary figure legends**



617

618 **Fig. S1.** Geographic distribution of the B.1.1.7 variant. Heatmap of the geographic
619 distribution of B.1.1.7 isolates retrieved from the GISAID EpiCoV database as of 28th June,
620 2021.

621

622

623

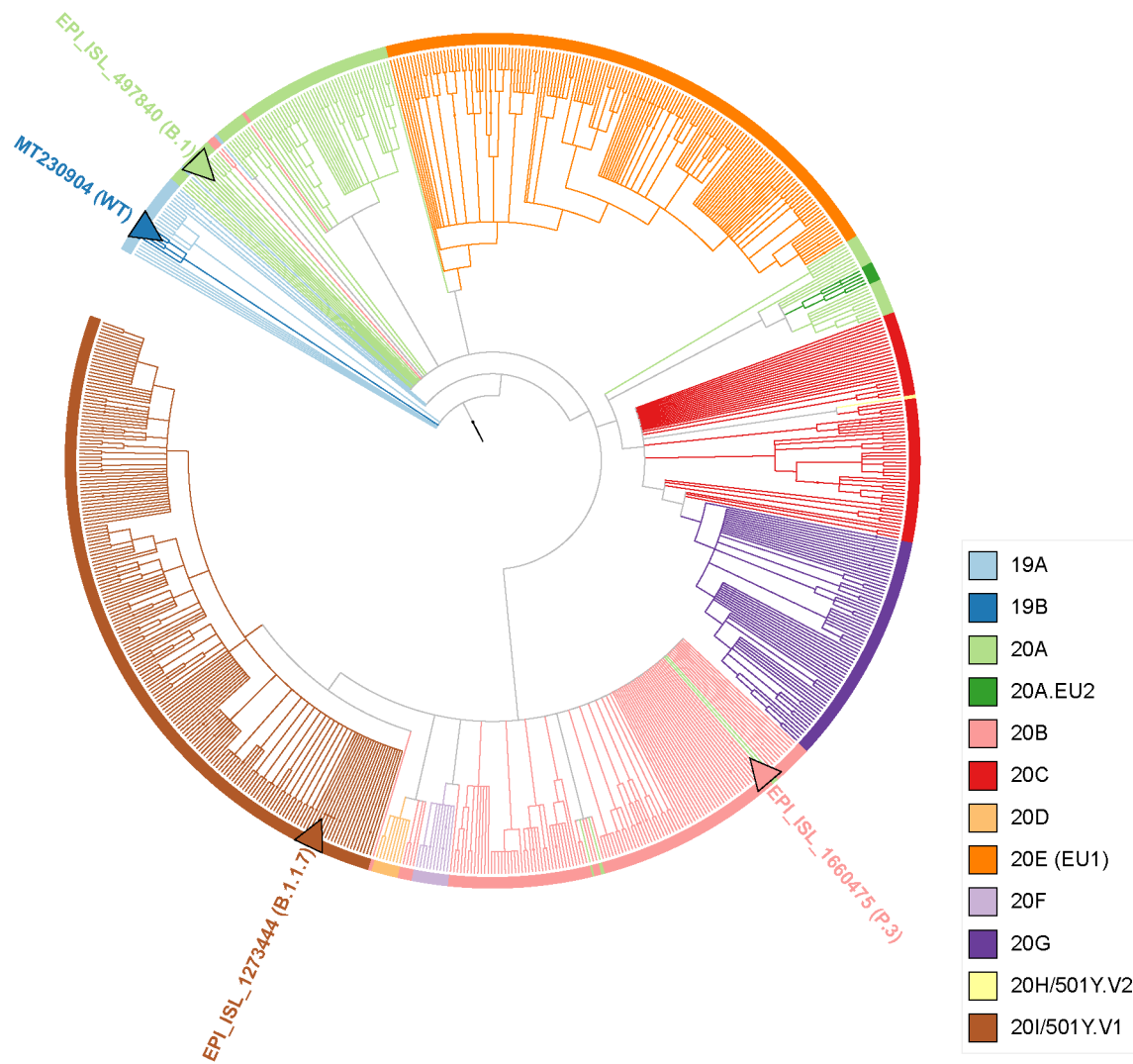
624

625

626

627

628

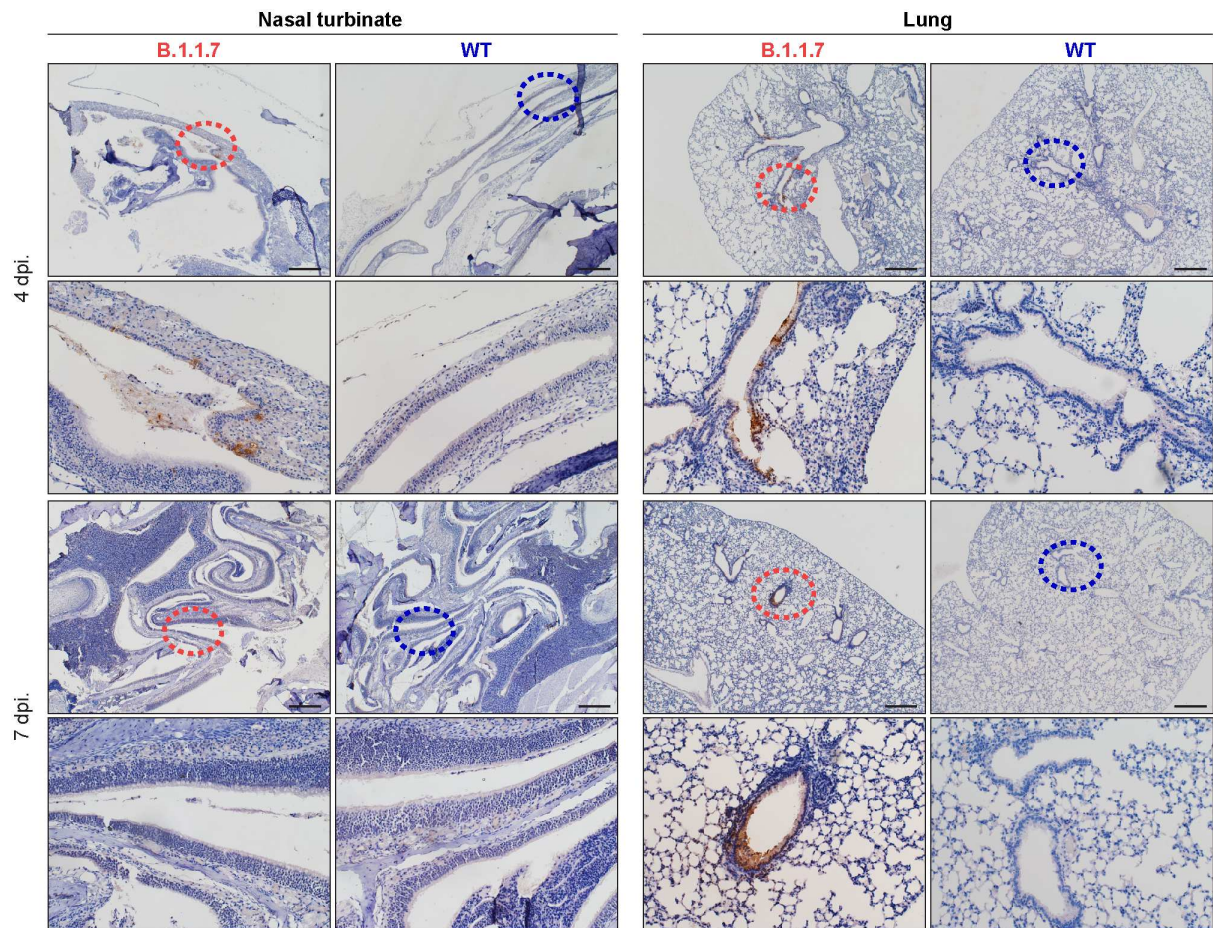


629

630

631 **Fig. S2. Phylogenetic tree of virus strains used in this study.** Phylogenetic tree showing
 632 evolutionary position of the wild type SARS-CoV-2 (Genbank: MT230904), SARS-CoV-2
 633 variant B.1 (GISAID: EPI_ISL_497840), B.1.1.7 (GISAID: EPI_ISL_1273444), and P.3
 634 (GISAID: EPI_ISL_1660475) as of 15th April, 2021. To place the four SARS-CoV-2
 635 sequences in the existing phylogenetic tree, full-length sequences were uploaded to UshER
 636 with default parameters. The phylogenetic tree including genomes from GeneBank, COG-UK
 637 and CNCB as of April 15, 2021. Phylogenetic tree follow-up modification was done in iTOL.

638



639

640

641 **Fig. S3. Immunohistochemistry staining of nasal turbinates and lungs from SARS-CoV-**

642 **2-inocuated C57B6 mice.** Representative images of immunohistochemistry staining for the

643 detection of SARS-CoV-2 nucleocapsid protein (brown) in the nasal turbinates (left) and lung

644 (right) from B.1.1.7- or WT SARS-CoV-2-inoculated mice on 4 d.p.i. and 7 d.p.i.. Insets

645 were shown for the circled areas. Scale bar, 500 μ m.

646

647

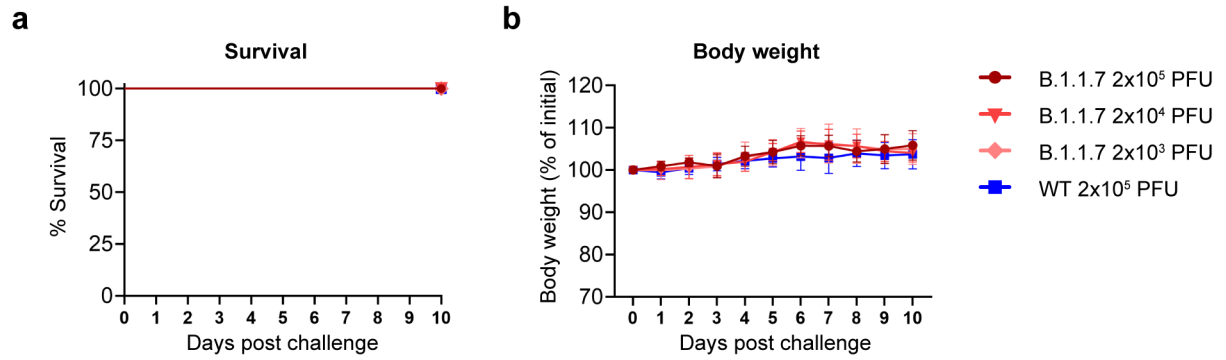
648

649

650

651

652



653

654 **Fig. S4. Survival and body weight of C57B6 mice infected with B.1.1.7 variant.** C57B6

655 mice were intranasally inoculated with 2×10^5 PFU WT SARS-CoV-2 or with B.1.1.7 at

656 2×10^3 , 2×10^4 or 2×10^5 PFU. **(a)** Mice survival and **(b)** body weight changes were shown until

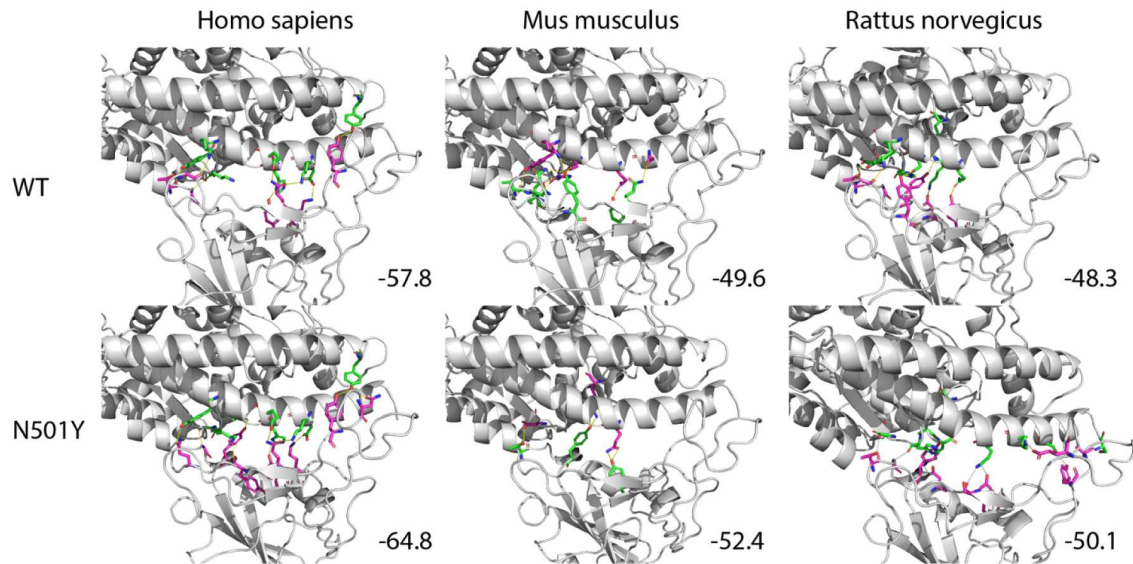
657 10 d.p.i..

658

a

Sequence variation of ACE2 residues interacting with SARS-CoV-2 spike RBD																				
Species	24	27	28	30	31	34	35	37	38	41	42	79	82	83	330	353	354	355	357	393
Homo sapiens	Q	T	F	D	K	H	E	E	D	Y	Q	L	M	Y	N	K	G	D	R	R
Mus musculus	N	.	.	N	N	Q	T	S	F	.	H
Rattus norvegicus	K	S	.	N	.	Q	I	N	F	.	H

b



659

660 **Fig. S5. Interaction between SARS-CoV-2 spike RBD and ACE2. (a)** Sequence alignment

661 of the interface residues from ACE2 proteins of human, mouse, and rat that are within 4.0Å

662 of RBD. The dots indicate amino acid residues that are identical to that of human. **(b)**

663 Binding mode and energy of ACE2 proteins from different species with wild type and

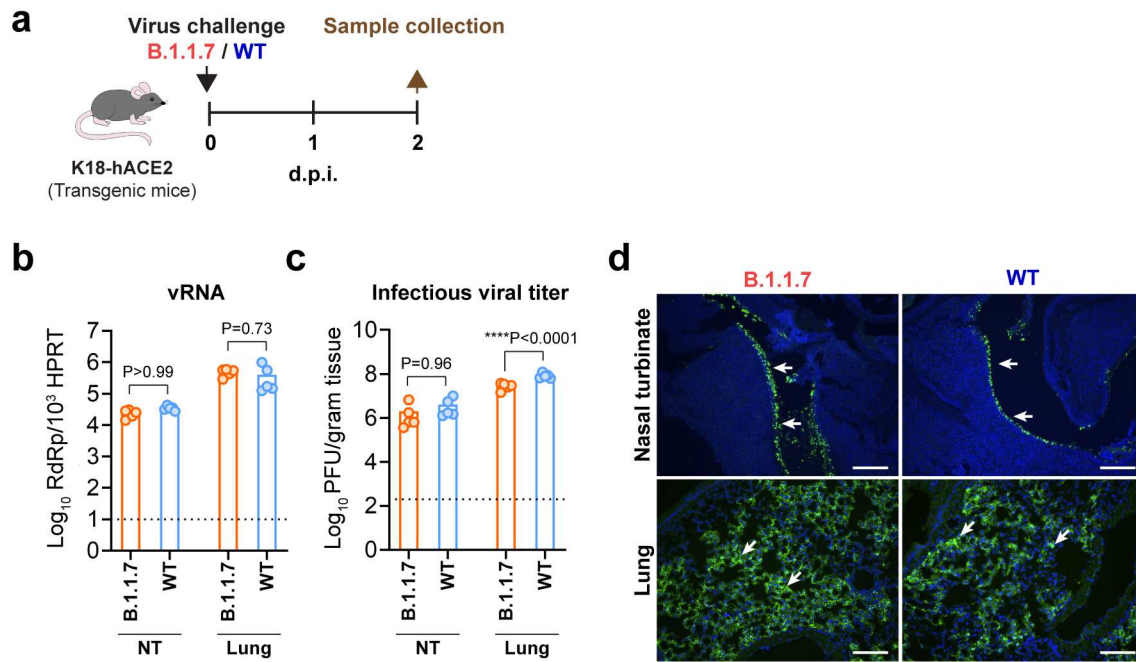
664 N501Y RBD. ACE2 and RBD were shown in gray cartoon representation. Polar interactions

665 were indicated with yellow dotted lines. Polar interaction partners from ACE2 and RBD were

666 shown as green and magenta sticks. The predicted binding affinities were labelled

667 accordingly.

668



669

670 **Fig. S6. B.1.1.7 and WT SARS-CoV-2 infection in K18-hACE2 mice.** (a) Schematic
 671 illustration of the infection experiment. (b) Virus genome copy quantified with RT-qPCR in
 672 the nasal turbinate and lung. NT, nasal turbinate. (c) Infectious virus titer quantified with
 673 plaque assays in the nasal turbinate and lung. (d) Representative images of
 674 immunofluorescence staining to show the expression of nucleocapsid protein (green, white
 675 arrows) in the lung and nasal turbinates. Scale bar, 200 μ m. Statistical differences were
 676 determined with two-tailed Student's t-test in (b) and (c). * represented $P < 0.05$; **
 677 represented $P < 0.01$; *** represented $P < 0.001$; **** represented $P < 0.0001$. NT, nasal
 678 turbinates.